J. Fluid Mech. (2010), *vol.* 660, *pp.* 37–54.
doi:10.1017/S0022112010001047

Mean flow deformation in a laminar separation bubble: separation and stability characteristics

OLAF MARXEN[1,2]† AND ULRICH RIST[1]

[1]Institut für Aerodynamik und Gasdynamik, Universität Stuttgart, Paffenwaldring 21, 70550 Stuttgart, Germany

[2]Center for Turbulence Research, Stanford University, Stanford, CA 94305, USA

(Received 3 December 2008; revised 22 February 2010; accepted 25 February 2010; first published online 17 August 2010)

The mutual interaction of laminar–turbulent transition and mean flow evolution is studied in a pressure-induced laminar separation bubble on a flat plate. The flat-plate boundary layer is subjected to a sufficiently strong adverse pressure gradient that a separation bubble develops. Upstream of the bubble a small-amplitude disturbance is introduced which causes transition. Downstream of transition, the mean flow strongly changes and, due to viscous–inviscid interaction, the overall pressure distribution is changed as well. As a consequence, the mean flow also changes upstream of the transition location. The difference in the mean flow between the forced and the unforced flows is denoted the mean flow deformation. Two different effects are caused by the mean flow deformation in the upstream, laminar part: a reduction of the size of the separation region and a stabilization of the flow with respect to small, linear perturbations. By carrying out numerical simulations based on the original base flow and the time-averaged deformed base flow, we are able to distinguish between direct and indirect nonlinear effects. Direct effects are caused by the quadratic nonlinearity of the Navier–Stokes equations, are associated with the generation of higher harmonics and are predominantly local. In contrast, the stabilization of the flow is an indirect effect, because it is independent of the Reynolds stress terms in the laminar region and is solely governed by the non-local alteration of the mean flow via the pressure.

1. Introduction

In a flow along a rigid body with a sufficiently high Reynolds number, such as the straight wing of an unmanned aerial vehicle, layers of rotational flow occur close to the surface of the body. It is characteristic for these so-called boundary layers that only the upstream part of the flow determines its downstream development and not vice versa. This observation allows a mathematical description based on a parabolic set of partial differential equations: the boundary-layer equations (Prandtl 1904). The pressure remains constant in the wall-normal direction and the adjoining potential flow governs the evolution of the boundary layer via the pressure. Two distinct states of a boundary layer are observable: the laminar state and the turbulent state. The region marking the change from the laminar to the turbulent state is denoted the transition region.

† Email address for correspondence: olaf.marxen@stanford.edu

For a very strong adverse pressure gradient (APG), a boundary layer will detach from the wall, resulting in boundary-layer separation. In the definition of separation, we follow Weldon *et al.* (2008), who derived their definition from ideas of Prandtl (1904). The pressure of the irrotational potential flow is no longer merely imposed on the rotational, viscosity-dominated region. Instead, this region alters the potential flow considerably and with it the pressure distribution – a phenomenon denoted as viscous–inviscid interaction. As a result, the standard procedure of streamwise integration of the boundary-layer equations fails. Viscous–inviscid interaction in steady, laminar flow is well understood for cases where the separation region is small. An introduction can be found in Smith (1986) or Sychev *et al.* (1998), for instance. In contrast, various phenomena related to unsteadiness in separated flows are much less understood.

Both separation on the one hand and transition to turbulence on the other are seemingly two separate phenomena with no *a priori* relation. However, reattachment of a separated, initially laminar, boundary (or rather, shear) layer can occur because of an increase in momentum exchange in the wall-normal direction, induced through transition to turbulence. At the same time, laminar velocity profiles in a separation region possess an inflection point and are therefore much more unstable with respect to small disturbances than attached boundary layers. Occurrences of separation and transition are thus often linked: separation can enhance transition, while at the same time the resulting turbulence can reduce or terminate separation.

The resulting region from the point of separation S to reattachment R enclosing almost stagnant fluid in its upstream part is denoted a separation bubble. Following Gaster (1966), the expression laminar separation bubble (LSB) is used here even if the flow transitions before the mean reattachment.

Sandham (2008) applied a semi-empirical model, based on a coupling of the boundary-layer and the potential-flow equations, in order to study viscous–inviscid interaction in the flow over airfoils. At angles of attack where a laminar separation bubble occurred, he could observe a variation of transition and reattachment location associated with the oscillatory flow over an airfoil near stall. We will look into similar variations of these locations also caused by viscous–inviscid interaction, while explicitly capturing the transition.

In the following, mean flow shall denote a flow field one obtains from averaging in time. For three-dimensional calculations, averaging is also carried out in the homogeneous spanwise direction. More precisely, the term mean flow corresponds to the existence of a steady state of the flow field, at least in a statistical sense, so that the time interval $[t_{st}, t_{st} + T_{aver}]$ used for averaging has no influence on the result irrespective of the choice of its beginning t_{st} and duration T_{aver}. Here only (quasi-) time-periodic flows will be considered, in which case multiples of the fundamental period will be used to reduce the required time T_{aver}.

Mean flow deformation (MFD) denotes a change of the averaged flow field with respect to another mean state of the flow. Therefore, at least two statistically steady states of the same flow field must exist. They can be, for instance, generated through different unsteady forcing which vanishes in the mean so that the mean boundary conditions are identical. If one of the flow states is fully laminar (even at reattachment and beyond), the time average is equal to any instantaneous realization. Such a situation is considered in this paper. If no steady-state solution exists or is known, MFD corresponds to the difference between two different statistically steady-state solutions.

In an LSB, the effect of MFD can be applied for flow-control purposes to reduce the size of the bubble; see for instance Marxen, Kotapati & You (2006) and Rist &

Augustin (2006). However, the underlying physical mechanisms are not yet well understood, which provides the motivation for the present paper. The effect of mean flow deformation is inherently a nonlinear effect: considering the Navier–Stokes equations for the mean flow, it can be seen that MFD is caused through the action of the Reynolds stress terms.

Boiko, Dovgal & Hein (2008) investigated the effect of steady spanwise perturbations in the separated flow behind a backward-facing step. They found a spanwise-modulated modification of mean velocity gradients of the separated flow. Note that their definition of a mean flow distortion only involves time, but not spanwise, averaging and is therefore different to the definition of MFD we use in this paper. They found an alteration of the local stability characteristics with regard to unsteady perturbations. They observed a peak–valley splitting, suggesting that in their case the unsteady perturbations are subject to a secondary instability.

A number of recent investigations have studied laminar separated flows within a global stability framework (e.g. Ehrenstein & Gallaire 2008; Marquet *et al.* 2008). The study reported here differs from these investigations in two important aspects. First, our base flow is not globally unstable. Second, we focus on nonlinear effects so that our interpretations may, in principle, hold for arbitrarily large deviations from a certain laminar base state. Applying a weakly nonlinear analysis, Sipp & Lebedev (2007) investigated the change in global stability caused by the mean flow deformation for a circular cylinder and an open cavity theoretically. They showed that the mean flow deformation alters both the instability and the separation regions.

2. Numerical method and set-up

2.1. *Numerical method*

To generate a base flow for subsequent investigations of transitional flow, a steady-state solution is obtained using an ADI method initially developed by Kloker (1993). An adverse pressure gradient is induced via the streamwise velocity u at the upper boundary y_{max}. At the inflow x_{ifl}, a self-similar solution is prescribed. The computation is advanced in time until a steady state, the base flow, is reached.

Next, runs are carried out in disturbance formulation, i.e. the base flow is kept frozen and enters the computation only via the nonlinear terms. The incompressible time-dependent three-dimensional Navier–Stokes equations in vorticity–velocity formulation are solved on a Cartesian grid using a high-order finite-difference method (Kloker 1998). This method has been applied in several studies of transitional flow (e.g. Bake, Meyer & Rist 2002; Wassermann & Kloker 2003). In the present formulation, a transport equation is solved for each of the three vorticity components. The wall-normal velocity component is computed from a Poisson equation while the spanwise mean part of the streamwise velocity component results from an integration of the continuity equation, from inflow to outflow. At the inflow, disturbances are set to zero. A buffer zone at the outflow serves to avoid reflections from disturbances that leave the domain. No-slip/impermeability conditions apply on the plate ($y = 0$). The spanwise direction z is periodic and the equations are solved in Fourier space with a fundamental spanwise wavelength λ_z (spanwise Fourier harmonics are denoted by their wavenumber coefficient k).

Disturbances are triggered via blowing/suction at the wall (i.e. through the wall-normal velocity) within a disturbance strip $[x_{st}, x_{en}] = [1.1525, 1.2834]$ with a certain

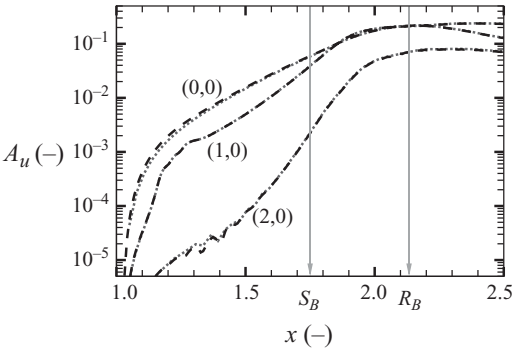

FIGURE 1. Amplification curves for the maximum (in y) streamwise velocity fluctuation $A_u = |\hat{u}'^{(h,k)}_{max}|$. Results from two-dimensional simulations with disturbance input $A_v^{(1,0)} = 4 \times 10^{-4}$ for domain heights $y_{max} \approx 40\,\delta^*_{ifl}$ (dashed line) and $y_{max} \approx 60\,\delta^*_{ifl}$ (dotted line).

fundamental frequency $\beta_0 = 2\pi/T_0$, a time harmonic h and an amplitude A_v:

$$\hat{v}(t, x, k)|_{y=0} = \begin{cases} \mathscr{F}_{ds}(x)\, A_v(h, k)\, \sin(h\beta_0 t)), & x \in [x_{st}, x_{en}], \\ 0, & x \notin [x_{st}, x_{en}]. \end{cases} \tag{2.1}$$

Here, $\mathscr{F}_{ds}$ denotes a smooth streamwise distribution assuming values in the interval $[-1, 1]$. The choice of the circular frequency was guided by a stability analysis of the base flow (Rist & Maucher 1994; Rist, Maucher & Wagner 1996). Here, it was set to $\beta_0 = 18.0$, which is close to the most (convectively) amplified frequency. In a real-world application, the true source of such a disturbance may be for instance acoustic noise, originating in the free stream or at the trailing edge of an airfoil. The interaction of this noise with the leading edge of the airfoil or a rough surface upstream of the APG region may then create boundary-layer disturbances of the type generated here by blowing and suction at the wall, but the details of such a receptivity process are outside the scope of this paper.

A boundary-layer interaction model is required at the upper boundary to render simulation results independent of the domain height as shown in figure 1 (see also Marxen 2005). This model can be interpreted such that the streamwise velocity u at the upper boundary is known (Dirichlet condition for u), and then the continuity equation yields the derivative for v. A non-homogeneous Neumann boundary condition for the wall-normal velocity is applied as an upper boundary condition using the streamwise derivative of u to prescribe a $\partial v/\partial y$:

$$\partial\hat{v}(t, x, k = 0)/\partial y = c(x) = \partial\hat{u}(x, y_{max}, k = 0)/\partial x \quad \text{for } t \to \infty. \tag{2.2}$$

Thereby, $\hat{u}$ is computed from the boundary-layer interaction model. The integration domain must be large enough so that the unsteady disturbance evolution for $k = 0$ close to the wall is not affected by the condition of vanishing unsteadiness at the upper boundary. Note that the streamwise velocity is not fixed *a priori* but results from the boundary-layer interaction model (for details see Marxen 2005). The actual values of the wall-normal velocity at the free-stream boundary are thus a solution of the method, with the final streamwise distribution of values becoming independent of time. The aim of this procedure is that in every case, the same slip-flow distribution is obtained, independent of the disturbance which is forced. The boundary-layer interaction model has been validated against experimental results (Marxen 2005). A decay condition is used for the spanwise-varying Fourier modes.

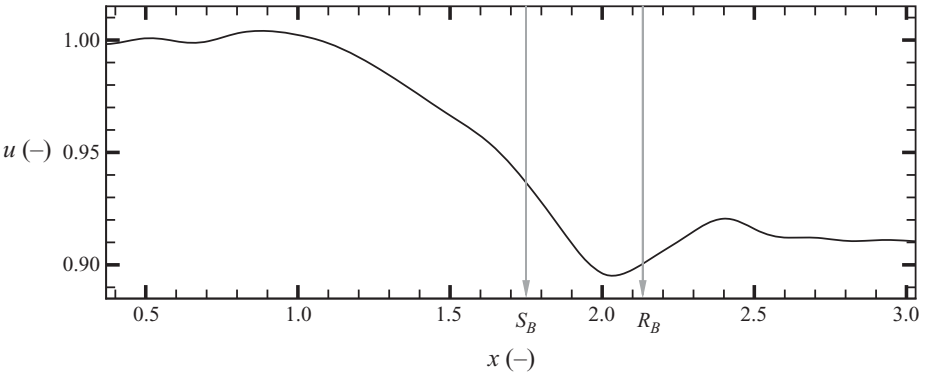

FIGURE 2. Streamwise velocity distribution u_e (base flow) prescribed at $y_{max,hd} = 72\,\delta^*_{ifl}$.

2.2. *Set-up: base flow and disturbance flow*

The basic configuration is given by a flat-plate boundary layer at a sufficiently high Reynolds number subjected to a streamwise pressure gradient. This pressure gradient is presumably caused by putting a displacement body into the flow at some distance from the wall. The body is assumed to be sufficiently far away from the wall and small in size that the flow keeps its semi-bounded character – in contrast to e.g. a channel flow. Numerical results from two-dimensional and three-dimensional simulations will be discussed, of which the three-dimensional results can be considered as direct numerical simulations (DNS). The APG is sufficient to cause a region of enclosed reversed flow, which we will call the separation region. At the same time, it is small enough that we obtain laminar reattachment within a short streamwise distance.

The base flow shall fulfil two main criteria in order to be suitable for our purposes. First, the region of reversed flow shall be sufficiently small to not introduce any absolute or global instabilities. Second, the adverse pressure gradient shall be strong enough to induce a notable viscous–inviscid interaction. Comparing the perturbed mean flow and the unperturbed steady-state flow then allows us to obtain a very clean representation of the effects of the viscous–inviscid interaction. Once a good understanding of this interaction has been achieved, results obtained for different forcing amplitudes can be more easily interpreted. This latter procedure – comparing e.g. the mean flows obtained with different forcing amplitudes – is applicable even in more strongly separated flows (Marxen & Henningson 2007), where a steady state is not straightforward to attain, and the first criterion can be relaxed. Here, we restrict ourselves to the mildly separated case.

All quantities are normalized by a dimensional reference length $\tilde{L}_{ref}$ and a reference velocity (free-stream speed at the inflow) $\tilde{U}_\infty$. The global Reynolds number is $Re_{global} = \tilde{U}_\infty \tilde{L}_{ref}/\tilde{\nu} = 10^5$. The origin of the coordinate system is placed at the (virtual) origin of the flat plate.

To obtain the base flow, at the inflow $x_{ifl} = 0.37$ a Blasius boundary-layer profile is prescribed with a Reynolds number based on the displacement thickness of $Re_{\delta^*} = \tilde{U}_\infty \tilde{\delta}^*/\tilde{\nu} = 331$. Even though in the following figures the (arbitrary) reference length has been used, a conversion to a normalization length scale based on the displacement thickness at the inflow can easily be done by multiplying the respective quantity, for instance the streamwise axis, by a factor of $Re_{global}/Re_{\delta^*} \approx 300$. In the wall-normal direction, the domain from the wall at $y = 0$ to $y_{max} = 72\,\delta^*_{ifl}$. The computational grid used to compute the steady state for $y_{max} = 72\delta^*_{ifl}$ is 385 equidistant points in the wall-normal direction and 2786 points in the streamwise direction. The prescribed distribution $u(x, y_{max} = 72\delta^*_{ifl})$ at the upper boundary is given in figure 2.

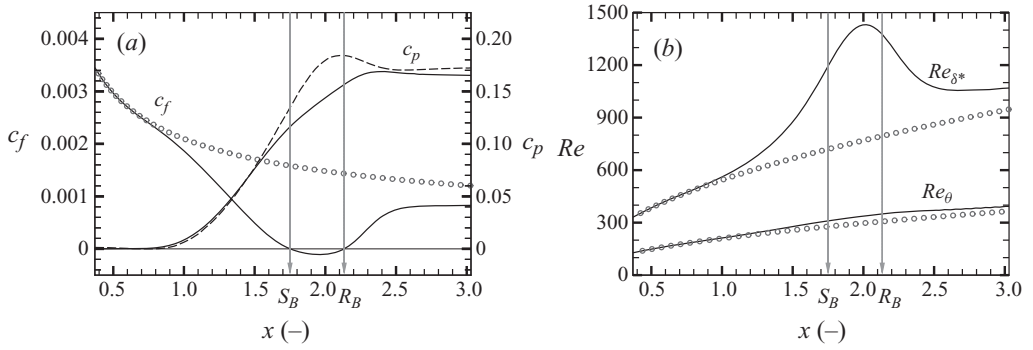

FIGURE 3. Coefficients for surface pressure c_p, skin friction c_f (*a*), and Reynolds numbers based on the displacement thickness Re_{δ^*} and on the momentum thickness Re_θ (*b*). Comparison of base-flow values (solid lines), the Blasius values for $u_e \equiv 1$ (symbols) and slip flow results $c_{p,slip}$ (dashed line).

The motivation behind this distribution is to obtain the best possible match of the steady state with results of Rist & Maucher (1994) and Rist *et al.* (1996) while at the same time using a four times larger domain. Details on how this distribution was derived can be found in Marxen (2005).

The unperturbed flow, generated using the ADI method, remained in a steady state and exhibited no sign of vortex shedding. Similarly, when switching off the disturbance input in the simulations with unsteady forcing using the disturbance formulation and explicit time stepping, two-dimensional and three-dimensional perturbations in the flow field decayed over time and the field returned to the unperturbed base state (Rist *et al.* 1996). This is considered as evidence that our base flow is globally stable and that our method did not artificially suppress unforced vortex shedding. Moreover, those results suggested that any possibly occurring reflections at the outflow boundary are sufficiently small to not contaminate the solution in the separation region.

For the unsteady simulations, the steady state was interpolated onto a finer, stretched grid with 225 grid points in y and a shorter domain $x \in [1.0216, 3.647]$ was used. The upper boundary is located at $y_{max} = 0.132 \approx 40\delta^*_{ifl}$. It was checked that this shortening did not affect the region of interest around the location of the separation bubble (details for the streamwise shortening can be found in Appendix A.3 of Marxen 2005, and for the wall-normal shortening in § 5.2.2 of the same reference). In the three-dimensional case, the number of spanwise Fourier modes is 63 and the spanwise wavenumber $\gamma = 2\pi/\lambda_z = 40.0$.

To reproduce the present study experimentally, a tunnel with a very low turbulence level would be required. Moreover, a suitable contoured upper ceiling or a displacement body, examples of which are given by Watmuff (1999) and Lang, Rist & Wagner (2004), could be used to generate a matching pressure gradient. Not only the inviscid c_p at the wall (figure 3) but also the inviscid u_e at a certain distance from the wall reported here (figure 2) should help to create an initial design of the shape of the ceiling/displacement body. The final design then would have to be adjusted in an iterative way, as a boundary layer also occurs on this body and probably would have to be sucked off (Lang *et al.* 2004). Alternatively, a rounded backward-facing step could be used. Bestek, Gruber & Fasel (1993) related their numerical configuration, which is similar to the present one, to such a step. Bao & Dallmann (2004) demonstrated experimentally that a steady-state laminar separation bubble can indeed be obtained on a rounded step (see their figure 9, upper).

Reproducing the present results numerically would require the usage of an interactive upper boundary condition similar to the one used here or in Maucher, Rist & Wagner (2000). Another possibility would be to use a very large domain. The difficulty in the latter approach would be to match the present pressure gradient at the wall (or the boundary-layer edge), and would most likely require a trial-and-error procedure.

2.3. *Post-processing*

All boundary-layer quantities derived from DNS such as the displacement thickness δ^* and the momentum thickness θ are computed using a pseudo velocity. Following Spalart & Strelets (2000), this pseudo velocity u_{psd} is obtained from a wall-normal integration of the spanwise vorticity ω_z.

To track the streamwise evolution of a forced disturbance and its nonlinearly generated harmonics, a double Fourier transform in time and spanwise direction (the latter only for three-dimensional computations) yields disturbance amplitudes and phases. Throughout this paper, the notation (h, k) will be used to specify modes, with h and k denoting wavenumber coefficients in time and spanwise direction, respectively.

3. Interaction of the separation bubble and forced perturbations

The set-up follows the one that has been studied before by Rist & Maucher (1994), Rist *et al.* (1996) and Marxen (2005). Therefore, only a brief description is given below.

3.1. *Description of the steady-state base flow*

A tiny, shallow separation bubble develops on the plate. The maximum reverse-flow intensity is $u_{r,max} \approx 1\,\%$. Figure 3 shows the streamwise development of important boundary-layer parameters. In this and the following figures, S_B and R_B mark the separation and reattachment location of the steady (laminar) base flow, index B, respectively. Despite the bubble being small, a notable difference to the pressure distribution of a corresponding inviscid flow (denoted as slip flow) is visible. Compared to a flat plate, a strong increase in the quantities related to the displacement of the boundary layer (such as δ^*, Re_{δ^*}) can be seen. Only far downstream of separation is a Blasius boundary layer formed again.

We believe that for the effects considered in this paper, the present LSB can be regarded as representative of boundary layers with strong or sudden pressure gradients up to those with a significant amount of reverse flow due to separation. Some evidence for the latter case can be found in Marxen & Henningson (2007). Note that the non-local effects that will be described below are associated with an elliptic behaviour and cannot be captured by the parabolic boundary-layer equations (if no interactive boundary condition is used).

3.2. *Comparison of the steady-state base flow and the disturbed flow*

Three different cases, two two-dimensional cases and one three-dimensional simulation, will be considered below. Only in the three-dimensional simulation (details of which can be found in Marxen 2005), is full breakdown to turbulence achieved by forcing a disturbance with $A_v^{(1,1)} = 4 \times 10^{-4}$. The difference between the two two-dimensional cases lies in the forcing amplitude ($A_v^{(1,0)} = 4 \times 10^{-4}$ versus $A_v^{(1,0)} = 4 \times 10^{-5}$). All calculations presented here are advanced until $T \geqslant 40\,T_0$, when initial transients have decayed sufficiently and a statistically steady state is

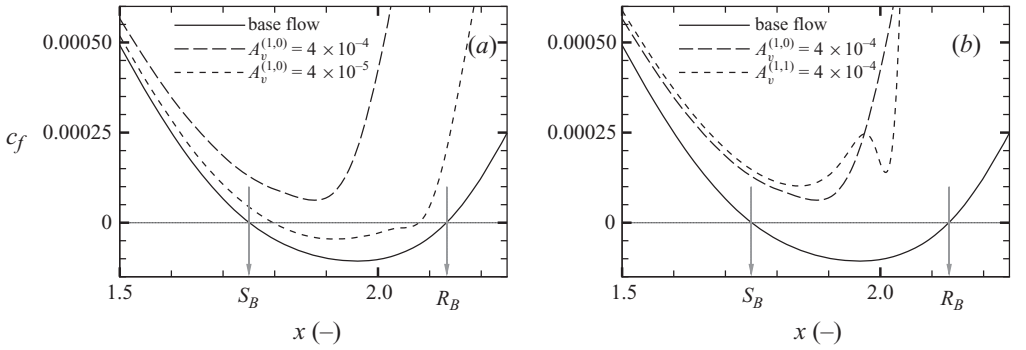

FIGURE 4. Skin-friction coefficient c_f for the different cases. (a) Two-dimensional cases with different forcing amplitudes and (b) two-dimensional versus three-dimensional simulation.

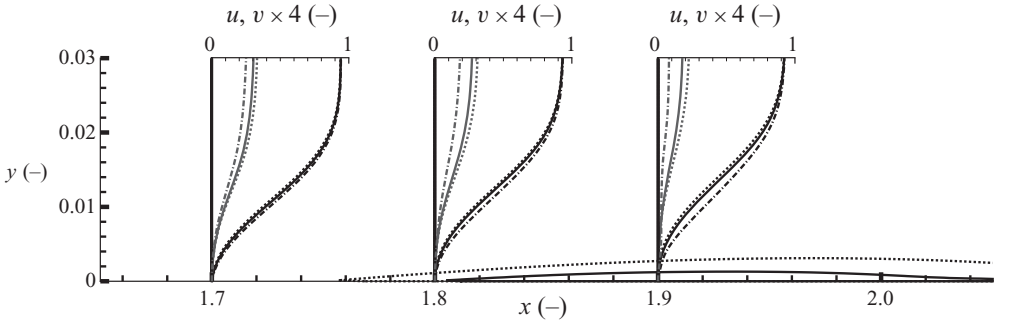

FIGURE 5. Profiles $u_B + \overline{u'}, v_B + \overline{v'}$ at $x = 1.7, 1.8, 1.9$ together with dividing streamlines $\psi_B + \overline{\psi'} = 0$ for disturbance input $A_v^{(1,0)} = 4 \times 10^{-5}$ (solid) and $A_v^{(1,0)} = 4 \times 10^{-4}$ (dash-dotted), base-flow quantities for reference (dotted). No bubble exists for $A_v^{(1,0)} = 4 \times 10^{-4}$.

reached. The interval for time averaging is chosen to be two periods of the forced perturbation.

3.2.1. *Influence of MFD on separation characteristics*

The disturbance input strongly affects the separation region. A strong rise in the skin friction can now be observed (figure 4) in between S_B and R_B. The position of this rise coincides approximately with the saturation location of the forced disturbances and their higher harmonics, e.g. mode (2, 0), as can be seen in figure 7. More important for the scope of this paper, however, is the observation that also upstream of this rise a difference in c_f compared to the base flow is visible already.

Only in the two-dimensional case with a very small disturbance input ($A_v^{(1,0)} = 4 \times 10^{-5}$) does the flow still separate. In this case, the separation bubble is shortened from both sides compared to the base flow (figure 4a). The entire bubble has become smaller, as can be seen from the mean dividing streamline $\overline{\psi}$ in figure 5. These observations, the bubble becoming smaller by being shortened from both sides, are consistent with observations reported in Rist & Augustin (2006) and Marxen *et al.* (2006) for entirely different cases, respectively.

Moreover, it can be seen in figure 5 that the larger the disturbance input, the closer the layer of strong $|\partial u/\partial y|$ moves to the wall. The wall-normal velocity at the edge of the boundary layer is reduced, too, and so is the displacement effect of the boundary layer.

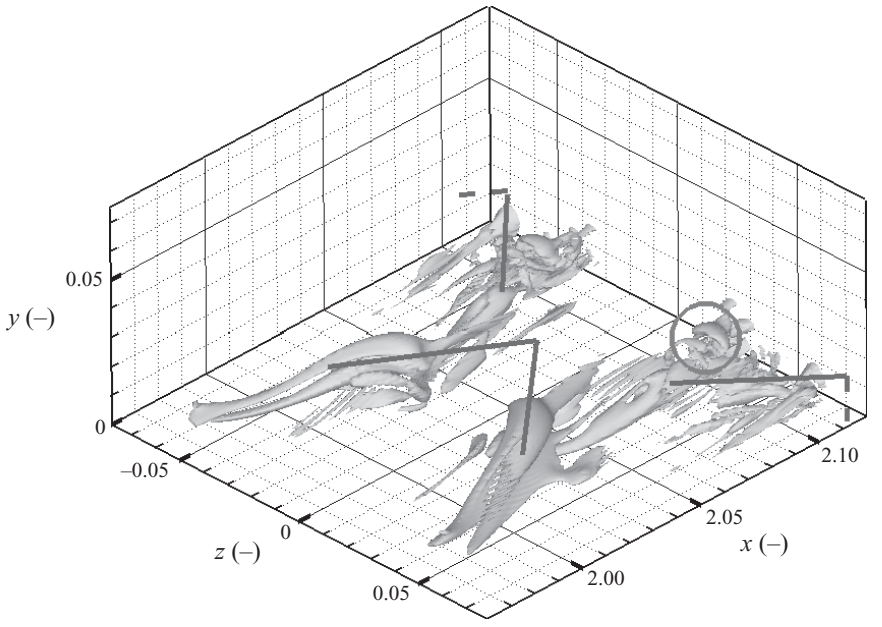

FIGURE 6. Isosurfaces of $\Lambda_2 = -125$ (vortex-visualization criterion by Jeong & Hussain 1995) from DNS at $t/T_0 = 25.0$ in the interval $(x, y, z) \in [1.96 \ldots 2.12, 0 \ldots 0.075, -\lambda_{z,0}/2 \ldots \lambda_{z,0}/2\,(\approx 0.0785)]$. Lines indicate the location of Λ-shaped vortices and a secondary vortex is marked by a circle.

No qualitative difference between the two-dimensional and the three-dimensional simulations occurs (figure 4*b*), in particular upstream of transition ($x < 2$). The strong rise observed in c_f is more pronounced in the three-dimensional case because in the three-dimensional simulation, the flow undergoes transition to small-scale turbulence. In the three-dimensional case, Λ-vortices appear during breakdown (figure 6), similar to observations of Alam & Sandham (2000), before they break down into smaller, secondary vortices. In the two-dimensional case, a mere shedding of large-scale spanwise rollers (vortices) occurs.

3.2.2. *Influence of MFD on linear stability characteristics*

Results of the Fourier analysis described in § 2.3 are given in figure 7 for one of the two-dimensional and the three-dimensional cases. The MFD in u corresponds to mode $(0, 0)$ in figure 7. The simulations are indeed converged to a periodic state as can be judged from the low level of subharmonic content mode $(0.5, 0)$, which is a remainder of the start-up. Because of the qualitative similarity of figures 7(*a*) and 7(*b*), only the three-dimensional case is considered below because it is the more realistic situation in practice.

Because the local linear stability properties of a boundary-layer velocity profile depend strongly on the distance of the shear layer from the wall (Rist *et al.* 1996), the movement of the shear layer observed in § 3.2.1 is expected to change the instability. To quantify this expectation, results for $A_v^{(1,1)} = 4 \times 10^{-4}$, where breakdown to turbulence occurs, shall be compared to a computation in which only a small-amplitude disturbance ($A_v^{(1,1)} = 4 \times 10^{-8}$) is forced such that the flow remains laminar throughout the domain.

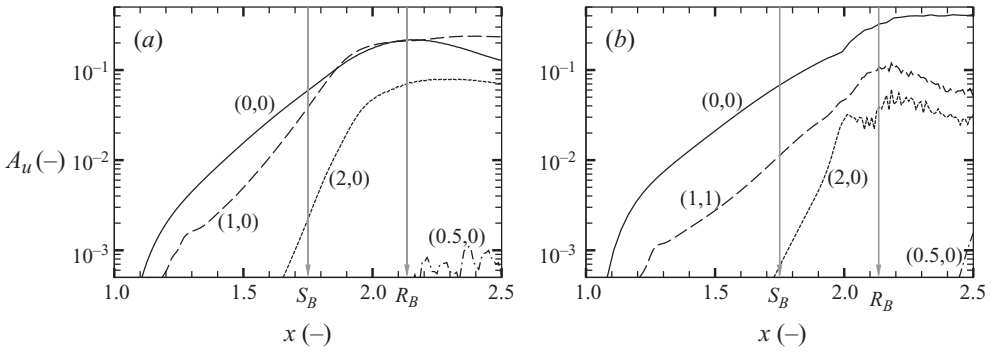

FIGURE 7. Amplification curves for the maximum (in y) streamwise velocity fluctuation $|\hat{u}'^{(h,k)}_{max}|$. (a) Two-dimensional simulation ($A_v^{(1,0)} = 4 \times 10^{-4}$) and ($b$) three-dimensional simulation ($A_v^{(1,1)} = 4 \times 10^{-4}$).

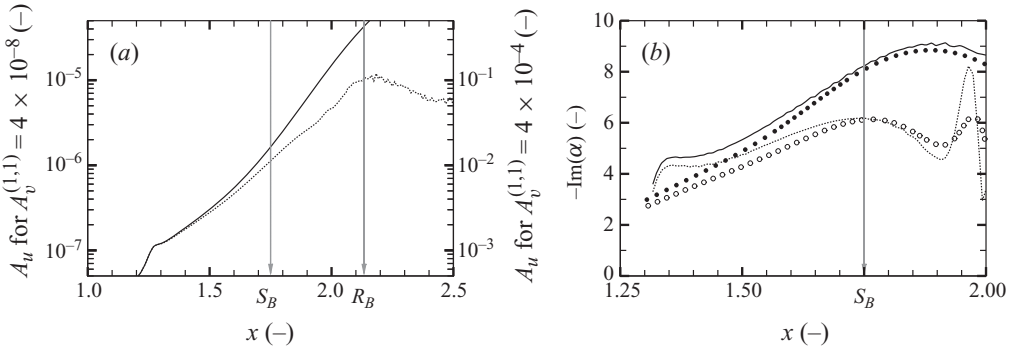

FIGURE 8. (a) Amplification curves for the maximum (in y) streamwise velocity fluctuation $|\hat{u}'^{(h,k)}_{max}|$. Results for $A_v^{(1,1)} = 4 \times 10^{-8}$ (solid line) and $A_v^{(1,1)} = 4 \times 10^{-4}$ (dotted line). (b) Amplification rate $\mathrm{Im}(\alpha^{(h,k)}_{DNS}) = -1/u^{(h,k)}\, \partial u^{(h,k)}/\partial x$ compared to linear stability theory (symbols) based on the respective mean flows. The line legend is the same as in (a).

Figure 8(a) shows that the flow field with larger disturbance input is more stable than the original base flow. Results from linear stability theory (LST), solving the Orr–Sommerfeld equation based on the respective time-averaged flows, confirm that indeed the linear stability properties have changed (figure 8b). The MFD has reduced the linear instability of the flow field notably: at $x = 1.75$ (which corresponds to S_B), a reduction in amplification rate of more than 26 % is observed. But even slightly downstream of the disturbance strip centred at $x = 1.218$, a small difference in growth rate is already visible.

3.3. *Physical mechanisms*

The observations in § 3.2 can briefly be summarized in the following way: MFD reduces separation and instability. This effect is visible already in the laminar part of the flow where the disturbance level is small. It shall be explained in the following.

3.3.1. *Mechanism responsible for the change in the mean flow*

Figure 7 shows that the MFD, mode (0, 0), is already larger than the disturbed modes (1, 0) or (1, 1) at the location of the disturbance strip. This observation can be explained by viscous–inviscid interaction. The strong displacement generated by the separation bubble alters the overall pressure gradient mostly in the vicinity of the bubble, as well as in the oncoming boundary layer before separation. If transition

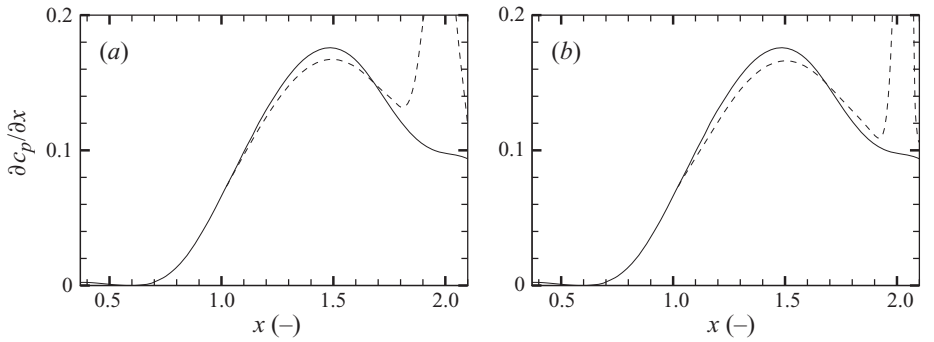

FIGURE 9. Coefficients for surface pressure gradient $\partial c_p/\partial x$. Results with disturbance forcing (dashed lines) for (*a*) the two-dimensional $A_v^{(1,0)} = 4 \times 10^{-4}$ and (*b*) three-dimensional $A_v^{(1,1)} = 4 \times 10^{-4}$ simulations together with base-flow values (solid lines). The scale of the plots has been chosen in a way to allow the best view of the area around the local maximum at $x \approx 1.5$. However, in the two-dimensional forced case, $\partial c_p/\partial x$ reaches values up to ≈ 0.26 and in the three-dimensional case up to ≈ 0.51.

causes the flow to reattach earlier, and therefore changes the displacement in the rear part of the bubble, this affects the flow upstream via an altered global pressure distribution.

On the basis of these considerations, the pressure gradient of the laminar base flow and the disturbed flow shall be compared for both a two-dimensional and the three-dimensional simulation. Figure 9 shows that with disturbance input, the pressure gradient is reduced by $\approx 5\,\%$ (two-dimensional) or $\approx 6\,\%$ (three-dimensional) (at $x \approx 1.5$) upstream of transition, while it is stronger downstream of it. The boundary layer possesses sufficient momentum to overcome the weaker pressure rise, and, as a result, it no longer separates with the forcing. Once the flow has transitioned, it can easily overcome a much stronger pressure rise without separating.

3.3.2. *Mechanism altering the linear instability and nonlinear effects*

The MFD, mode (0, 0), is a product of the quadratic nonlinearity of the Navier–Stokes equations, and so is its accompanying upstream effect, which is strongly dependent on the forcing amplitude (see figure 4*a*). On the other hand, favourable agreement of the forced mode (1, 1) with local linear theory has been observed in all cases as illustrated in § 3.2.2. Hence, the disturbance undergoes linear amplification in a region where the flow has been nonlinearly distorted.

To demonstrate that this is no contradiction, we have carried out an additional simulation (as in § 3.2.2, we consider only the three-dimensional case) with very small disturbance input $A_v^{(1,1)} = 4 \times 10^{-8}$. The base flow for this simulation is the flow field deformed by the MFD, i.e. the time-averaged total flow field from the simulation obtained with $A_v^{(1,1)} = 4 \times 10^{-4}$.

The small-amplitude simulation based on the deformed flow field exhibits the same amplification as the large-amplitude simulation up to $x = 1.65$ (this x value is based on visual inspection, figure 10*a*), i.e. we have linear behaviour up to that location. Downstream of this x-location, nonlinear saturation effects set in ('direct' effects) and the amplification rate for the large-amplitude (breakdown) simulation drops. But even at S_B ($x = 1.75$) the difference between the linear simulation based on the deformed flow field and the full nonlinear simulation (dashed versus dotted line) is much smaller than the difference between the linear simulations based on the deformed and the undeformed flow fields (dashed versus solid line), respectively.

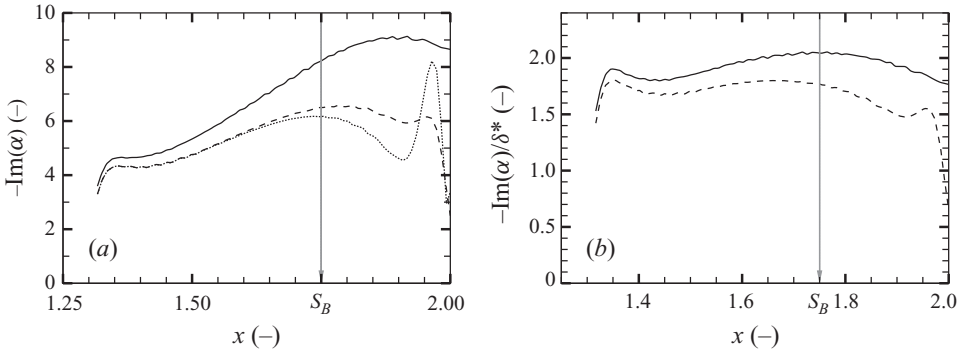

FIGURE 10. (*a*) Amplification rates $\mathrm{Im}(\alpha_{DNS}^{(1,1)})$ based on the maximum (in y) streamwise velocity fluctuation $|\hat{u}'^{(1,1)}_{max}|$. Results for $A_v^{(1,1)} = 4 \times 10^{-8}$ using the laminar base flow (solid line), the laminar base flow+MFD (dashed line) and for the reference case $A_v^{(1,1)} = 4 \times 10^{-4}$ (dotted line). (*b*) Same as (*a*), except that amplification rates are divided by the local boundary-layer displacement thickness δ^*. Line legend is the same as in (*a*).

To illustrate that the change in instability between the original base flow and the deformed mean flow is in part due to the wall-normal distance of the shear layer, we have normalized the amplification rates by the respective displacement thicknesses. The displacement thickness can be regarded as a certain measure for the distance of the shear layer from the wall. Figure 10(*b*) shows that at $x = 1.65$ the difference in amplification after normalization is only 16 % compared with 26 % before normalization (figure 10*a*). Another influence is most likely the differences in shapes of the velocity profiles.

We summarize that we have observed two types of nonlinear effects: 'direct' saturation effects and 'indirect' effects related to the change of the stability via altered mean-flow profiles (i.e. MFD), caused by a change in the overall pressure distribution. Indirect effects could be evaluated (for $x \lesssim 1.65$) from a comparison of both calculations with $A_v = 4 \times 10^{-8}$ (the solid and dashed lines in figure 10*a*) and are therefore independent of the disturbance amplitude at the locations where we observe them. As this effect is caused by an event (the transition) further downstream, we can also denote this effect as non-local. In contrast, direct effects require the disturbance to reach a certain threshold amplitude and were visible from a comparison of the linear computation using the time-averaged flow field (i.e. the base flow+MFD) with the one of oblique breakdown (the dashed and dotted lines in figure 10*a*). This effect is initiated at the position where the disturbance amplitude becomes large and is thus a local effect.

4. Discussion

As indicated in the introduction, our results may have implications not only for flow control but also for related tasks such as transition/separation prediction. These implications shall be discussed in the following.

4.1. *The feedback loop*

The main feature of the effect of MFD is the non-local change of the pressure gradient via viscous–inviscid interaction caused by disturbance input in the first place. As a result, the pressure gradient, boundary-layer evolution and disturbance amplification are all coupled via this interaction: we have a situation with loop character.

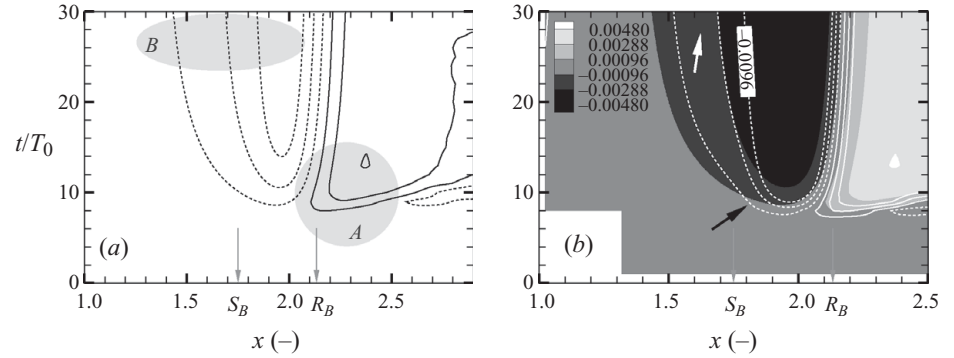

FIGURE 11. (*a*) Contours of v_{vis} (black lines) as defined in (4.1). Contour levels span the interval $[-0.0048{,}0048]$ with a spacing of 9.6×10^{-4}. Negative contours are dashed. (*b*) Contours of q (white lines) as defined in (4.3), with a spacing of 19.2×10^{-4}, together with contours of v_{vis} (grey scale).

The feedback loop occurs in space, namely in the streamwise direction. However, to better illustrate this feedback loop, we consider the temporal evolution in the three-dimensional case during the start-up of the simulation. When we start with the steady-state solution and ramp up the disturbance input, a wave packet is generated and convected downstream. The wave (of the packet) belonging to the forcing frequency travels into the undisturbed flow, where it gets amplified with an amplification rate according to linear stability theory based on the undisturbed flow.

As soon as the disturbance reaches large amplitudes, breakdown to turbulence occurs. The resulting turbulent boundary layer causes (initially) a stronger displacement than the laminar boundary layer in place before. To quantify this viscous displacement, we will consider the following quantity, based on the spanwise-averaged wall-normal velocity at the upper boundary y_{max} of the simulation in disturbance formulation (therefore, it is denoted by a prime $'$):

$$v_{vis}(t, x) = \frac{1}{t} \int_0^t \hat{v}'_{k=0}(\tau, x, y_{max})\, \mathrm{d}\tau. \tag{4.1}$$

Note that v_{vis} will converge towards the mean flow deformation $v_{MFD} = \hat{v}^{(0,0)}$ if $\hat{v}'_{k=0}$ becomes stationary. As a result of the breakdown and the associated stronger displacement, v_{vis} is positive towards the rear part of the bubble (figure 11*a*), and it peaks at $t/T_0 \approx 13$ (see the circular region labelled A in figure 11*a*) before levelling off.

Compared to the rear part, a response in v_{vis} in the front part of the LSB is slightly delayed. The quantity v_{vis} is negative there, because the bubble shrinks and disappears. Eventually, its rate of change decreases (i.e. the slope of the contours becomes steeper, see region labelled B) and the flow gradually approaches a statistically steady state.

As in thin airfoil theory (Schlichting & Truckenbrodt 2001), a continuous source/sink distribution $q = q(x)$ at the wall $y = 0$ shall be defined. This distribution q shall generate the same wall-normal velocity v_{vis} as the boundary layer in the irrotational free stream, i.e. at y_{max}:

$$v_{vis}|_{y_{max}} = \frac{1}{2\pi} \int_{x_{ifl}}^{x_{ofl}} \frac{y_{max}}{(x-\xi)^2 + {y_{max}}^2}\, q(\xi)\, \mathrm{d}\xi \doteq \int_{x_{ifl}}^{x_{ofl}} \mathscr{G}(x-\xi, y_{max})\, q(\xi)\, \mathrm{d}\xi \doteq \mathscr{G} \circ q. \tag{4.2}$$

To obtain q for a given v_{vis}, the convolution operation is inverted approximately by the van Cittert method (Bertero & Boccacci 1998), with $\mathscr{G}$ defined according to (4.2):

$$q = \mathscr{G}^{-1} \circ v_{vis}|_{y_{max}} \approx \sum_{p=0}^{15} (1-\mathscr{G})^p \circ v_{vis}|_{y_{max}} \quad \text{with} \quad \mathscr{G}^p \circ v_{vis}|_{y_{max}} = \underbrace{\mathscr{G} \circ \mathscr{G} \circ \ldots}_{p \text{ times}} \circ v_{vis}|_{y_{max}}. \tag{4.3}$$

In order to evaluate the error caused by the approximative nature of (4.3) and the choice of using 15 terms for the sum, we looked at the location of the maximum absolute difference between v_{vis} and v^*_{vis}, where v^*_{vis} is obtained from (4.2) using the resulting q from (4.3). At this location, the relative error $|(v^*_{vis} - v_{vis})/v_{vis}|$ remained below ≈ 0.07 (7 %).

Initially, when the flow in the rear part of the bubble strongly changes, this leads to an immediate change in the source/sink distribution q (figure 11*b*), including the region of separation. The boundary layer in the front part of the bubble can now be viewed as to be subject to the action of 'suction' ($q < 0$) – or, from a different point of view, a less severe pressure gradient. Note that while the change in q occurs immediately, the boundary-layer response in the front region of the LSB lacks behind because of viscous effects, so that we have a clear qualitative difference in contours v_{vis} and q at early times (see the black arrow in figure 11*b*), at which the contours of q and v_{vis} cross each other instead of running roughly at a constant distance from each other.

As the disturbance forcing is continued with a fixed amplitude, the boundary layer will eventually adapt to the new pressure gradient in a way so that separation is delayed to a position further downstream or even completely suppressed. Therefore, after a sufficient amount of time has passed, we not only see a qualitative similarity of contours v_{vis} and q_{MFD}, but we also have $q_{MFD} \approx 2v_{vis}$ (except around the extrema of v_{vis}) as in thin airfoil theory (see the white arrow in figure 11*b*).

Eventually, all disturbances that leave the strip and enter the APG boundary layer get slightly less amplified (i.e. according to the amplification rate of the new mean flow), but will still cause transition. At long times, the flow has settled and attained the periodic, fully coupled state observed in our simulations.

Although the interpretation given above has been based on the velocity v_{vis} at the top boundary y_{max} of the particular integration domain used in the simulation, additional checks showed that it is independent of the specific choice of y_{max}. Our interpretation therefore holds for a semi-infinite domain in the wall-normal direction.

4.2. *The possible role of MFD with respect to flapping, vortex shedding and global modes*

It is understood that the settlement mentioned in the previous section relies on a constant forcing amplitude, and it will take a certain time until this state is reached. This led Marxen (2005) to argue that the described loop-type situation could be responsible for flapping, if the disturbance input is not held at a constant amplitude. Such a situation is common in practice (free flight) and it may occur in experiments when transition is not forced explicitly. For example, if the forcing had been switched off at $t/T_0 = 30$, the flow would return to the fully laminar state after an additional time of $t/T_0 \approx 40$, as it can be estimated based on the results of Rist *et al.* (1996). Then, by switching the forcing on again, we could repeat the cycle and hence cause a low-frequency oscillation of the mean flow.

In the literature, evidence exists that mono-harmonic forcing with a fixed amplitude can reduce flapping significantly, see for instance Dovgal & Boiko (1994) and figure 1.3, p. 6, in Lang (2005). Investigations by Sandham (2008) also suggested an interconnection of viscous–invisicd interaction and flapping.

The LSB considered here can be classified as convectively unstable and hence it is globally stable. Nevertheless, the scenario of a repeated excitation as just described resembles the repeated reappearance of a localized wave packet considered in Ehrenstein & Gallaire (2008). In this sense, during the start-up of our simulation, the initial wave packet may lead to an excitation of a global mode (which is stable, and hence we have a subcritical excitation). On the other hand, our results have demonstrated the importance of nonlinearity, while the global stability analysis of the type presented in Ehrenstein & Gallaire (2008) relies on a linearization around the steady base flow. Further investigations are necessary in order to come to a definite conclusion.

The spanwise rollers in the two-dimensional case mentioned before are similar to those vortices often shed from LSBs during shear-layer breakdown caused by a Kelvin–Helmholtz instability (for an example of this type of vortex shedding, see Marxen *et al.* 2003). However, the present LSB is small and even entirely disappears once a certain forcing amplitude is reached. Thus, the role the rollers play in the reattachment process – and hence in the feedback loop – (also) requires further investigations in more strongly separated flows.

Beside the vortex shedding caused by a Kelvin–Helmholtz instability, which often occurs in conjunction with an explicit forcing, a second type of shedding appears to exist. This second type remains much less understood and has been observed in many cases without explicit forcing (e.g. Pauley, Moin & Reynolds 1990; Rist & Maucher 2002; Ehrenstein & Gallaire 2008; Jones, Sandberg & Sandham 2008). Different explanations for this type of shedding have been proposed or at least investigated, including an absolute local instability similar to wake flows (Rist & Maucher 2002; Jones *et al.* 2008), a global instability (Ehrenstein & Gallaire 2008), viscous–inviscid interaction (Sandham 2008) and insufficient convergence in numerical solution schemes (Rist & Maucher 2002).

Our present results can make a contribution to this discussion in that they indicate that one should take into account the nonlinear contribution of the mean flow deformation as an essential effect influencing the flow stability. A theoretical approach similar to the global weakly nonlinear analysis used by Sipp & Lebedev (2007) may provide further insight into the vortex-shedding dynamics for pressure-induced laminar separation bubbles.

4.3. *The role of MFD with respect to separation/transition studies*

The present results suggest that studies of linear instability for a convectively amplified perturbation in the laminar forepart of an LSB must be based on the deformed, i.e. the finally resulting, flow field rather than on an entirely laminar base flow. Examples in support of this assertion include the Kelvin–Helmholtz instability (Lang *et al.* 2004) and Görtler instability/spatial transient growth (Marxen *et al.* 2009), where good agreement of linear results with an experiment was observed, respectively. In most cases, using the deformed field is a natural choice because a fully laminar flow is not available or might not even exist, as in the case of an experiment. Note that not only is the amplification rate changed for a fixed frequency but in fact the entire linear stability diagram becomes a function of the forcing; for an example see Marxen *et al.* (2006).

Our results for two-dimensional and three-dimensional forcing indicate that two-dimensional simulations are able to qualitatively capture the important features of MFD in short laminar separation bubbles. Nevertheless, three-dimensional simulations are necessary if one wishes to obtain the best possible accuracy in terms of e.g. size and position of the LSB to compare simulation results with experimental data or for the design of technical devices.

4.4. *The role of MFD with respect to separation/transition prediction*

Because of the feedback loop described in § 4.1, it is difficult to accurately predict not only the transition but also the separation location. For instance, an approach based just on LST or the linear parabolized stability equations (PSE; for an example see Hein 1999) with a given steady-state flow will not yield an amplitude dependence of the separation location as it does not capture either the 'direct' or the 'indirect' nonlinear effect of MFD. But even nonlinear PSE will only be able to account for the 'direct' nonlinear effect. Hence, for the most accurate prediction, an interactive coupling has to be included to reflect the feedback loop.

This may be achieved for instance by a combination of nonlinear PSE with an interactive upper boundary condition to alter the mean flow (and an iterative reintegration of the boundary-layer equations). For weak deviations from a certain reference condition, a global weakly nonlinear approach (Sipp & Lebedev 2007) may offer another option.

5. Conclusions

The mutual influence of mean-flow separation and disturbance amplification in a laminar separation bubble has been investigated. Forced disturbances, which are convectively amplified downstream, develop into large-scale structures and promote earlier reattachment or remove the separation region completely. Because of the inviscid–viscous interaction, this change in the mean flow downstream of the transition location changes the overall pressure distribution and with it the laminar boundary layer in the part upstream of the transition location. In turn, this changes the amplification rate of a small, linear convectively amplified disturbance in the laminar part. This loop-type situation can be summarized as follows: because of transition, the separation region becomes smaller from both sides or is even completely removed, which in turn causes a (simultaneous) reduction in the linear amplification rate of the initially small disturbances that later cause the transition.

The effect of MFD is inherently nonlinear and non-local, i.e. global. More precisely, two different types of nonlinear effects were found. While the MFD at and downstream of transition is caused directly, or locally, via the nonlinearity of the Navier–Stokes equations, the mean flow deformation upstream is induced indirectly, or non-locally, via a change in the streamwise pressure distribution caused by the saturated disturbances.

Our results also suggest that it may be instructive to consider a two-dimensional simulation as a starting point for investigations of laminar separation bubbles, as the present two-dimensional simulations were able to capture already the fundamental effects of the interaction between mean flow and disturbance. Because of quantitative differences and the risk of missing inherent three-dimensional effects, in particular differences in vortical structures at transition, they cannot entirely replace three-dimensional simulations.

Financial support for this research by the Deutsche Forschungsgemeinschaft (German research foundation) under grant Ri 680/10-1 and Ma 3916/1-1 is gratefully acknowledged.

REFERENCES

Alam, M. & Sandham, N. D. 2000 Direct numerical simulation of 'short' laminar separation bubbles with turbulent reattachment. *J. Fluid Mech.* **410**, 1–28.

Bake, S., Meyer, D. G. W. & Rist, U. 2002 Turbulence mechanism in Klebanoff transition: a quantitative comparison of experiment and numerical simulation. *J. Fluid Mech.* **459**, 217–243.

Bao, F. & Dallmann, U. 2004 Some physical aspects of separation bubble on a rounded backward-facing step. *Aerosp. Sci. Technol.* **8** (2), 83–91.

Bertero, M. & Boccacci, P. 1998 *Introduction to Inverse Problems in Imaging*. Institute of Physics Publishing.

Bestek, H., Gruber, K. & Fasel, H. 1993 Direct numerical simulation of unsteady separated boundary-layer flows over smooth backward-facing steps. In *Physics of Separated Flows – Numerical, Experimental and Theoretical Aspects* (ed. K. Gersten). Notes on Numerical Fluid Mechanics, vol. 40, pp. 73–80. Vieweg.

Boiko, A. V., Dovgal, A. V. & Hein, S. 2008 Control of a laminar separating boundary layer by induced stationary perturbations. *Eur. J. Mech.* B/*Fluids* **27** (4), 466–476.

Dovgal, A. V. & Boiko, A. V. 1994 Effect of harmonic excitation on instability of a laminar separation bubble on an airfoil. In *Laminar–Turbulent Transition* (ed. H. Fasel & W. Saric), pp. 675–680. Springer.

Ehrenstein, U. & Gallaire, F. 2008 Two-dimensional global low-frequency oscillations in a separating boundary-layer flow. *J. Fluid Mech.* **614**, 315–327.

Gaster, M. 1966 The structure and behaviour of laminar separation bubbles. *AGARD* CP–4, pp. 813–854.

Hein, S. 1999 Linear and nonlinear non-local instability analyses for two-dimensional laminar separation bubbles. In *Laminar–Turbulent Transition* (ed. H. F. Fasel & W. S. Saric), pp. 681–686. Springer.

Jeong, J. & Hussain, F. 1995 On the identification of a vortex. *J. Fluid Mech.* **285**, 69–94.

Jones, L. E., Sandberg, R. D. & Sandham, N. D. 2008 Direct numerical simulations of forced and unforced separation bubbles on an airfoil at incidence. *J. Fluid Mech.* **602**, 175–207.

Kloker, M. 1993 Direkte numerische Simulation des laminar-turbulenten Strömungsumschlages in einer stark verzögerten Grenzschicht. Dissertation, Universität Stuttgart, Stuttgart, Germany.

Kloker, M. 1998 A robust high-resolution split-type compact FD scheme for spatial direct numerical simulation of boundary-layer transition. *Appl. Sci. Res.* **59**, 353–377.

Lang, M. 2005 Experimentelle Untersuchungen zur Transition in einer laminaren Ablöseblase mit Hilfe der Laser-Doppler-Anemometrie und der Particle Image Velocimetry. Dissertation, Universität Stuttgart, Stuttgart, Germany.

Lang, M., Rist, U. & Wagner, S. 2004 Investigations on controlled transition development in a laminar separation bubble by means of LDA and PIV. *Exp. Fluids* **36**, 43–52.

Marquet, O., Sipp, D., Chomaz, J.-M. & Jacquin, L. 2008 Amplifier and resonator dynamics of a low-Reynolds-number recirculation bubble in a global framework. *J. Fluid Mech.* **605**, 429–443.

Marxen, O. 2005 Numerical studies of physical effects related to the controlled transition process in laminar separation bubbles. Dissertation, Universität Stuttgart, Stuttgart, Germany.

Marxen, O. & Henningson, D. S. 2007 Direct numerical simulation of the bursting of a laminar separation bubble and evaluation of flow-control strategies. In *IUTAM Symposium on Unsteady Separated Flows and Their Control'* June 18–22, Kerkyra (Corfu), Greece (ed. M. Braza & K. Hourigan). Springer.

Marxen, O., Kotapati, R. B. & You, D. 2006 Evaluation of active control of a laminar separation bubble based on linear stability theory. In *Annual Research Briefs 2006*, pp. 323–335. Center for Turbulence Research, Stanford University.

Marxen, O., Lang, M., Rist, U., Levin, O. & Henningson, D. S. 2009 Mechanisms for spatial steady three-dimensional disturbance growth in a non-parallel and separating boundary layer. *J. Fluid Mech.* **634**, 165–189.

Marxen, O., Lang, M., Rist, U. & Wagner, S. 2003 A combined experimental/numerical study of unsteady phenomena in a laminar separation bubble. *Flow Turbulence Combust.* **71**, 133–146.

Maucher, U., Rist, U. & Wagner, S. 2000 Refined interaction method for direct numerical simulation of transition in separation bubbles. *AIAA J.* **38** (8), 1385–1393.

Pauley, L. L., Moin, P. & Reynolds, W. C. 1990 The structure of two-dimensional separation. *J. Fluid Mech.* **220**, 397–411.

Prandtl, L. 1904 Über Flüssigkeitsbewegung bei sehr kleiner Reibung. In *Verhandlungen des dritten Internationalen Mathematiker-Kongresses in Heidelberg vom 8. bis 13. August 1904.* (Proc. 3rd Intl Math. Congr., Heidelberg, Germany, August 8–13, 1904).

Rist, U. & Augustin, K. 2006 Control of laminar separation bubbles using instability waves. *AIAA J.* **44** (10), 2217–2223.

Rist, U. & Maucher, U. 1994 Direct numerical simulation of two-dimensional and three-dimensional instability waves in a laminar separation bubble. In *Proc. 74th Fluid Dynamics Symposium on Application of Direct and Large Eddy Simulation to Transition and Turbulence*, *AGARD* CP–551, pp. 34.1–34.7. AGARD

Rist, U. & Maucher, U. 2002 Investigations of time-growing instabilities in laminar separation bubbles. *Eur. J. Mech.* B/*Fluids* **21**, 495–509.

Rist, U., Maucher, U. & Wagner, S. 1996 Direct numerical simulation of some fundamental problems related to transition in laminar separation bubbles. In *Computational Fluid Dynamics '96* (ed. J.-A. Désidéri, C. Hirsch, P. L. Tallec, M. Pandolfi & J. Périaux), pp. 319–325. Wiley.

Sandham, N. D. 2008 Transitional separation bubbles and unsteady aspects of aerofoil stall. *Aeronaut. J.* **112** (1133), 395–404.

Schlichting, H. & Truckenbrodt, E. 2001 *Aerodynamik des Flugzeuges*, 3rd edn. Springer.

Sipp, D. & Lebedev, A. 2007 Global stability of base and mean flows: a general approach and its applications to cylinder and open cavity flows. *J. Fluid Mech.* **593**, 333–358.

Smith, F. T. 1986 Steady and unsteady boundary layer separation. *Annu. Rev. Fluid Mech.* **18**, 197–220.

Spalart, P. R. & Strelets, M. K. 2000 Mechanisms of transition and heat transfer in a separation bubble. *J. Fluid Mech.* **403**, 329–349.

Sychev, V. V., Ruban, A. I., Sychev, V. V. & Korolev, G. L. 1998 *Asymptotic Theory of Separated Flows*, 1st edn. Cambridge University Press.

Wassermann, P. & Kloker, M. 2003 Transition mechanisms induced by travelling crossflow vortices in a three-dimensional boundary layer. *J. Fluid Mech.* **483**, 67–89.

Watmuff, J. H. 1999 Evolution of a wave packet into vortex loops in a laminar separation bubble. *J. Fluid Mech.* **397**, 119–169.

Weldon, M., Peacock, T., Jacobs, G. B., Helu, M. & Haller, G. 2008 Experimental and numerical investigation of the kinematic theory of unsteady separation. *J. Fluid Mech.* **611**, 1–11.